

BASED: Bundle-Adjusting Surgical Endoscopic Dynamic Video Reconstruction using Neural Radiance Fields

Shreya Saha¹, Sainan Liu², Shan Lin¹, Jingpei Lu¹, and Michael Yip¹

Abstract—Reconstruction of deformable scenes from endoscopic videos is important for many applications such as intraoperative navigation, surgical visual perception, and robotic surgery. It is a foundational requirement for realizing autonomous robotic interventions for minimally invasive surgery. However, previous approaches in this domain have been limited by their modular nature and are confined to specific camera and scene settings. Our work adopts the Neural Radiance Fields (NeRF) approach to learning 3D implicit representations of scenes that are *both dynamic and deformable* over time, and furthermore with unknown camera poses. We demonstrate this approach on endoscopic surgical scenes from robotic surgery. This work removes the constraints of known camera poses and overcomes the drawbacks of the state-of-the-art unstructured dynamic scene reconstruction technique, which relies on the static part of the scene for accurate reconstruction. Through several experimental datasets, we demonstrate the versatility of our proposed model to adapt to diverse camera and scene settings, and show its promise for both current and future robotic surgical systems^{*}.

I. INTRODUCTION

Surgical scene reconstruction from endoscopic videos is an important and challenging task in robotic-assisted minimally invasive surgery [1]. It also has widespread use in many downstream clinical applications such as surgical workflow analysis, image-guided robotic surgery, automation, surgical environment simulation, and augmented reality to train surgeons to be familiar with an operative environment and reconstruction of tissues and organs for preoperative assessment and planning. Many learning and automation algorithms for robotic surgery are reliant on accurate 3D reconstruction of the surgical scenes [2].

The majority of current approaches for reconstructing surgical scenes from endoscopic videos adopt a modular sequence of tasks, each tackled by independent models [3]–[11]. This fragmented methodology is susceptible to accumulating errors and lacks efficient task coordination. For instance, a significant number of existing methods either estimate or rely on ground truth camera poses before proceeding with scene reconstruction. Errors in pose estimation often lead to faulty scene reconstructions. Camera poses obtained through structure from motion (SfM) or simultaneous localization and mapping (SLAM) [12]–[16] often exhibit noise. When the camera is fixed to the end effector of a robotic arm, camera pose estimation can be accomplished

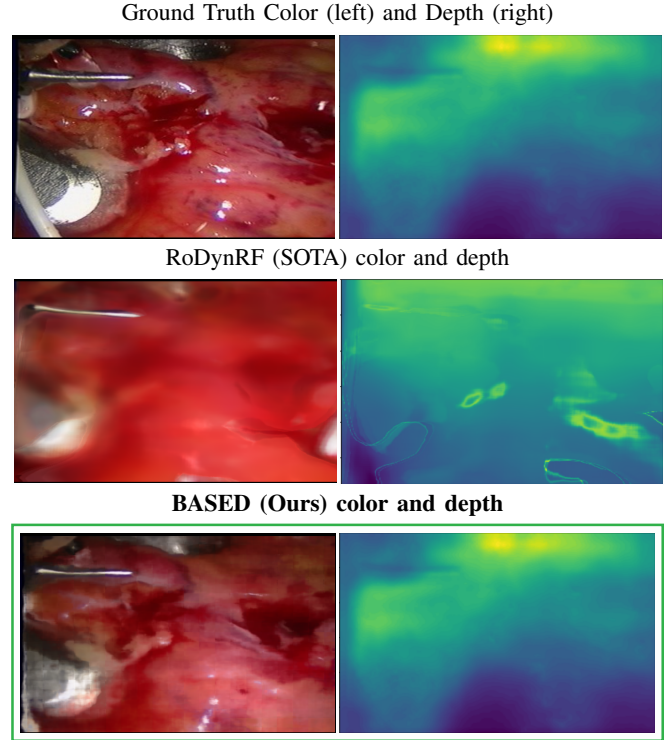


Fig. 1. BASED is a novel NeRF-based method that can be used in dynamic and deformable scenes with unknown camera poses. It can produce novel viewpoint renderings with robust color (left) and depth (right) reconstructions, even from monocular untracked camera images. Comparisons with state-of-the-art methods (RoDynRF shown above, EndoNeRF failed completely) show that it has leading performance in scene reconstruction. Depth in the ground truth row is the reference depth, estimated from [4].

through forward kinematics. However, these estimated poses are prone to errors stemming from inaccuracies in joint angle measurements attributed to instrument sag, cable stretch, positioning biases, and reading drift [17]. In reality, a further complication is that newer robotic systems are flexible, and these continuum robots (e.g., J&J Monarch Platform [18], Endomaster EASE System [19]) have complex mechanics that result in poor distal-camera localization. Furthermore, in addition to being modular, these methods will not generalize from static to deformable scene settings.

Neural Radiance Fields (NeRF) [20] has shown tremendous performance in the domain of 3D reconstruction. They have been applied recently to stereo-endoscopic videos for deformable surgery scene reconstruction [21], [22]. However, some constraints in these methods are that the camera should be static with stereo camera information and be in a known position. Alternatively, some works have extended NeRF with camera pose optimization (e.g., [23], [24]). However,

¹S. Saha, S. Lin, J. Lu, and M.C. Yip are with the Electrical and Computer Engineering Dept., University of California San Diego, La Jolla, CA 92093, USA. (e-mail: ssaha, shl102, jil360, yip@ucsd.edu), and ²S. Liu is with Intel Labs, USA. (e-mail: sainan.liu@intel.com).

^{*}Project Website: <https://sites.google.com/ucsd.edu/based-arclab-2023/>

these methods generally assume the scene to be static.

In this paper, we present the first NeRF-based method that can reconstruct deformable surgical scenes captured from untracked monocular endoscopic videos. The overall method combines a learnable pose layer that parameterizes camera poses, a deformation module that learns the deformation of a 3D point at a given time step with respect to a canonical position and a rendering module that takes the canonical coordinates of a 3D point at every time step along with the 2D camera directions and outputs the volumetric density and color information. We can solve for robotic surgical scene rendering of deforming scenes, even when the camera is a monocular camera, and in instances where the camera motion is unknown. This makes the method applicable to a wide range of robotic systems and semi-autonomous applications. The major contributions of this paper are thus:

- A NeRF approach for *dynamic and deformable* scenes from data captured at *unknown camera poses*,
- A method for describing multi-view correspondence loss, specifically catered to a dynamic and deformable setting, that enables establishing correspondence across spatiotemporal drift in tissues, and
- A framework that offers a generic, unrestricted, and versatile solution to robotic surgical perception that is validated on several surgical scene reconstruction datasets.

II. RELATED WORK

A. Traditional Scene Reconstruction Techniques

Structure from Motion (SfM) utilizes a series of two-dimensional images to construct a three-dimensional model of a scene or an object, and it is widely used in the domain of scene/organ/tissue reconstruction with endoscopic images [6]–[11]. However, SfM techniques like COLMAP [25], [26] often fail to estimate camera poses for the entire length of sequences and often change the sequence of images. Simultaneous localization and mapping (SLAM) is a technique used to build a map of an unknown environment while simultaneously estimating the camera’s position and orientation in the environment. SLAM-based approaches [12]–[16] have been employed in the field of endoscopic scene reconstructions to model sparse and dense tissue surfaces. The scene is usually assumed to be static, and the estimated deformations do not always look natural.

B. Static and Dynamic NeRF

NeRFs are implicit volumetric representations that encode the appearance and geometry of a 3D scene. It learns a continuous representation of the scene, enabling novel view renderings, as opposed to SLAM/SfM techniques that usually learn a discrete representation. It takes a 3D point coordinate and a 2D camera viewing direction and outputs RGB color information and the density of the point. The original NeRF model strictly catered to static scenes. D-NeRF [27] is the first work that expanded the NeRF model to learn deformable scenes. It consists of two separate models that progressively learn the deformation and the volumetric scene reconstruction simultaneously. Robust Dynamic NeRF,

or RoDynRF [28], tries to reconstruct dynamic scenes by estimating the camera poses using only the static part of the scene, which is not suitable for surgical scene reconstruction given that the scenes are highly deformable with a very low degree of rigidity. EndoNeRF [21] builds on D-NeRF for endoscopic scenes by adding a tool-guided ray casting and by sampling points along a ray closer to the tissue surfaces using a Gaussian transfer function but relying on stereo depth. EndoSurf [22] further improved upon EndoNeRF [21] by employing three networks to learn the deformation, signed distance function (SDF), and color of a viewpoint. However, as seen in Figure 1, these methods strictly cater to cases where the camera is static. If extended to moving camera sequences with camera poses estimated by COLMAP, the rendering quality degrades significantly.

C. Joint Pose Estimation and Scene Reconstruction

Bundle adjusting neural radiance fields (BARF) [29] first proposed an end-to-end NeRF-based framework that can jointly estimate camera extrinsics and reconstruct the 3D scene. It implements a coarse-to-fine technique to gradually activate the higher frequency components of the positional encoding scheme that aids in pose refinement, and only uses the photometric loss for backpropagation through the network. There have been numerous follow-up works ([23], [24], [30]–[36]) that improved BARF by optimizing its training time, adding prior losses and making it robust to in-the-wild sequences. However, all of these methods specifically deal with static scenes. RoDynRF is a recent paper, to the best of our knowledge, that has first implemented estimating camera poses while simultaneously reconstructing dynamic scenes. They combine the pose estimation module from BARF with the radiance field module of Dynamic NeRF [37]. Although RoDynRF’s problem formulation is similar to ours, it cannot be easily adapted in surgical scene settings, requiring the dynamic pixels to be masked out prior to training, where a motion mask is generated using Mask R-CNN [38] and optical flow [39]. This is hard to acquire as the entire surgical scene may be deformable and textureless. Hence, as seen in Figure 1, it cannot be generalized for endoscopic videos. Our proposed model overcomes the limitations of EndoNeRF and EndoSurf by expanding to moving cameras with unknown poses. It does not constrain part of the scene to be static for it to be able to learn deformations, thus also overcoming the limitations of RoDynRF.

III. METHODOLOGY

Figure 2 gives a high-level overview of our method. The overall model consists of three parts: (1) the pose estimation module (see III-A), (2) the deformable module (see III-B), and (3) a canonical NeRF module (see III-C).

A. Camera Pose Module

We use a camera pose module to model the appearance of the rigid-body motion of the scene either caused by a moving camera or moving scene as is shown in Figure 2 (A). We follow the convention of previous work [29] and

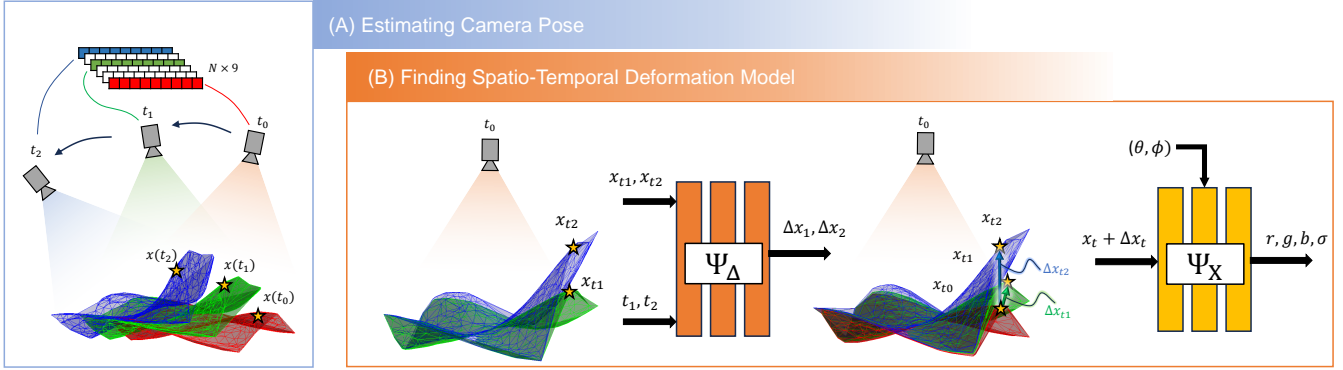


Fig. 2. Method overview: (A) The first part of the diagram shows a tissue that appears to be dynamic and deformable at three timestamps t_0 , t_1 , and t_2 . Camera poses are estimated by a $N \times 9$ learnable matrix through the camera pose estimation layer. $x(t_0)$, $x(t_1)$ and $x(t_2)$ shows the trajectory taken by the same point x on the tissue at these three different timesteps. (B) x_{t_1} and x_{t_2} represents non-rigid deformation trajectory of x at time t_1 and t_2 . The deformation model denoted by Ψ_Δ takes in x_{t_1} and x_{t_2} and predicts their displacement from the canonical configuration of the scene. The canonical model Ψ_x then takes in the mapped canonical position of the point $x_{t_0} = x_{t_1} + \Delta x_{t_1} = x_{t_2} + \Delta x_{t_2}$ along with 2D camera directions, and predicts the color and density information.

model the camera pose with $P_i = [R_i | t_i] \in SE(3)$ representing camera-to-world transform of camera i , where $R_i \in SO(3)$ denotes the rotation and $t_i \in \mathbb{R}^3$ denotes the translation. We use $K \in \mathbb{R}^{3 \times 3}$ to represent the intrinsic matrix.

In terms of implementation details, the poses are parameterized as a learnable parameter $P_i \in \mathbb{R}^9$ for $i \in [1, N]$ for N frames. The first six columns of the matrix refer to the first two rows of the camera rotation matrix, and the last three values refer to the camera translation vector. It should be noted that one can estimate the third row of the rotation matrix by taking a cross-product of the other two rows. The pose layer is initialized to identity and updated for the first 200 iterations, after which the layer is frozen.

B. Deformation Module

After the camera pose module explains away the rigid-body motion in the image, the deformation module will model the non-rigid-body deformation of the scene from a canonical state at t_0 as is shown in Figure 2 (B). The deformation module $\Psi_\Delta(x, t)$ takes as input 3D spatial coordinates $x \in \mathbb{R}^3$ and a time step t and learns the deformation Δx of the coordinate x from time step zero:

$$\Psi_\Delta(x, t) = \begin{cases} \Delta x & \text{if } t \neq 0 \\ 0 & \text{if } t = 0 \end{cases} \quad (1)$$

The idea is that the deformation can help us learn the position estimate of a point at the 0^{th} time interval, which will be assumed the canonical configuration. If x_0 is the coordinate of a point at time $t = 0$ and it deforms to x_t at time t , then we can say that $\Psi_\Delta(x_t, t) + x_t = x_0$.

C. Canonical NeRF Module

This module will capture the implicit 3D representation of the canonical state of the scene. The canonical module Ψ_x can be assumed to be a vanilla NeRF model, which takes as input a spatial 3D location and 2D camera orientations, and outputs color (RGB values) and the volumetric density of the location. x_0 calculated above is the input to the canonical model along with camera viewing directions d . The rendered

output of the canonical model (color c , and density σ) is corresponding to the deformed point x_t at time t .

$$\Psi_x(x_t + \Psi_\Delta(x_t, t), d) = c, \sigma \quad (2)$$

We apply conventional positional encoding [27] to all the inputs, $\langle (\sin(2^l \pi p), \cos(2^l \pi p)) \rangle_{>0}^L$, with $L = 10$ for 3D point coordinates x and time frame t , and $L = 4$ for camera directions d . For more information about volumetric rendering, please refer to the original NeRF paper [20].

D. Tool mask-guided ray casting and Stereo Depth Cue Ray Marching

Surgical tools occlude part of the scene in most of our sequences. Instead of shooting rays randomly all through the image, we adopt a tool mask-guided ray casting strategy [21]. Using binary tool masks, an importance map is created which highlights the regions containing tool pixels. During training, instead of random ray sampling throughout the image, we only sample pixels from this distribution using inverse transform sampling. Secondly, we sample pixels close to the tissue surface using a Gaussian transfer function and use a depth refinement strategy to get rid of corrupt artifacts in the estimated depths.

E. Losses

Our model uses photometric loss, correspondence loss, and estimated depth Loss for monocular dynamic camera deformable scene reconstruction.

RGB Photometric Loss: We use photometric loss based on conventional setup in NeRF models [20]. At every training iteration, we compare the rendered color of the sampled pixels with the ground truth colors using the L_2 loss, and this loss is backpropagated through the entire network with all three modules.

$$L_{pho} = \frac{1}{N} \sum_{i=1}^N \|\hat{C}_i(p, t) - C_i(p, t)\|_2^2 \quad (3)$$

where \hat{C}_i is the rendered color and C_i is the ground truth color of the pixel p at time t with respect to frame i , $i = 0 \dots N$.

Dynamic Multi-View Correspondence Loss: We introduce a novel 3D Multi-View correspondence loss for dynamic

Matching Pixels Taken from Different Viewpoints and Different Times

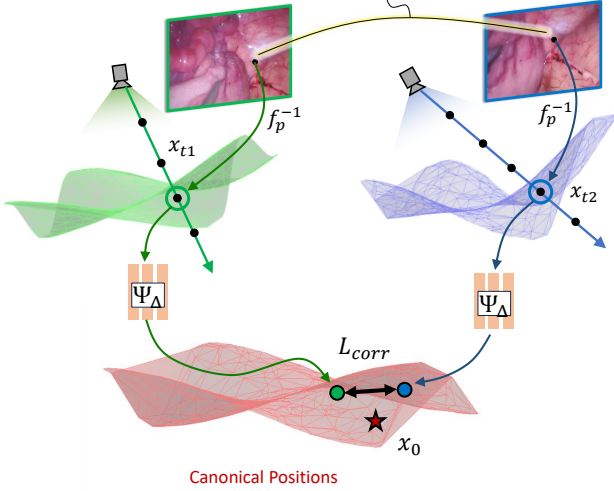


Fig. 3. Overview of the correspondence loss: Matching pixels are chosen from a random pair of images (having correspondence above a certain threshold) using PDC-Net [40]. The matching pixels are projected from 2D pixel space to their 3D positions in the world frame, and then further passed through the deformation model to get their canonical 3D positions. The difference between the mapped 3D points is used to calculate the flow correspondence loss. The loss is designed to pull the outputs of correspondence points returned by the deformation model closer together towards the same canonical point denoted as x_0 .

scenes to offer extra constraints on pose estimation. Figure 3 gives a high-level idea of this loss. For a given pair of images, I_i^a (viewpoint P_i at time t_a) and I_j^b (viewpoint P_j at time t_b) with matching pixels $p^a \in I_i^a$ and $q^b \in I_j^b$, both pixels p^a and q^b should project to the same point in 3D space in the canonical space. z_p^a and z_q^b are the estimated depths of the pixels p^a and q^b respectively. Let f_p^{-1} be the function that maps the 3D coordinate of a pixel given its estimated depth and its respective camera viewpoint. Let $x_p^a \in \mathbb{R}^3$ be the 3D coordinate of pixel p^a at time t_a and $x_q^b \in \mathbb{R}^3$ be the 3D coordinate of pixel q^b at time t_b . Then, the estimated coordinates are

$$x_p^a = f_{P_i}^{-1}(p^a, z_p^a) \quad (4)$$

$$x_q^b = f_{P_j}^{-1}(q^b, z_q^b) \quad (5)$$

If there was no deformation, x_p^a and x_q^b should be the same point in 3D space. However, since this is a deformable scene, we need to map both the points back to their canonical state in order to calculate the loss:

$$\hat{x}_p^a = \Psi_\Delta(x_p^a, t_a) + x_0 \quad (6)$$

$$\hat{x}_q^b = \Psi_\Delta(x_q^b, t_b) + x_0 \quad (7)$$

Then, the loss becomes:

$$L_{corr} = w(L_\delta(\hat{x}_p^a, \hat{x}_q^b)) \quad (8)$$

where w is loss weight term and L_δ is the Huber loss function.

Estimated Depth Loss: In spite of only having 2D images, we can use an *estimated* depth loss to further assist better reconstruction when the camera pose estimation is optimized. The depth estimates can be found via an off-the-shelf image-to-depth estimator. This loss is only used to optimize the

deformable and canonical modules after the pose layer is frozen. Applying the estimated depth loss before the camera pose matrix is optimized leads to abrupt artifacts. We collect depths estimated from RGB images via existing pre-trained methods [41], [4] during training. We compare the rendered depth values of the sampled pixels with the corresponding estimated depth values using a L_2 loss. The gradient from this loss is only backpropagated through the deformable NerRF modules, after the pose layer is frozen.

$$L_d = \frac{1}{N} \sum_{i=1}^N \|\hat{D}_i(p, t) - D_i(p, t)\|_2^2 \quad (9)$$

where $\hat{D}_i(p, t) = \frac{1}{\sigma_i(p, t)}$ is the rendered depth, σ_i is the rendered density and $D_i(p, t)$ is the reference depth of the pixel p at time t with respect to frame $i \in [1, N]$ for N frames. Note that if a hardware solution to depth is available (e.g., stereo cameras or RGB-D sensor), the ground truth depth can be used as well to calculate an estimated depth loss.

IV. EXPERIMENTS

A. Implementation Details

All of the experiments have been performed on a single Nvidia RTX-A6000 GPU. The weights of the NeRF network and the pose estimation network are simultaneously updated with a learning rate of $5e-4$. After 200 iterations, the pose layer is fixed, and only the NeRF model is updated for another 100K iterations. In the first stage, one batch consists of all of the training images, because it requires more views of the scene for better pose estimation. In the second stage, one batch consists of a single training image for faster training. Tool masks are manually created for the Hamlyn dataset sequences, partly using Segment Anything Model [42]. We use an off-the-shelf dense pixel correspondence network, PDCNet [43], to get corresponding matching pixels between a pair of images.

TABLE I. ABLATION STUDIES ON "RECTIFIED18-1" DATASET WITH DYNAMIC MOTIONS. ✓ INDICATES LOSS USAGE.

	BA	L_d	L_{corr}	PSNR↑	SSIM↑	LPIPS↓
EndoNeRF [21]	COLMAP	✓	-	26.97	0.895	0.164
BASED w/o $L_d L_{corr}$	✓	-	-	30.236	0.925	0.124
BASED w/o L_d	✓	-	✓	31.415	0.935	0.108
BASED w/o L_{corr}	✓	✓	-	31.403	0.937	0.102
BASED (final)	✓	✓	✓	32.227	0.944	0.106

BA stands for bundle-adjusting.

EndoNeRF experiment is using COLMAP for camera pose estimation.

B. Datasets

We evaluated BASED on the following datasets

Hamlyn Dataset [44]: We choose three videos from the Hamlyn dataset of robotic surgery with deformable scenes. Hamlyn dataset contains weak textures, and the scene is often occluded by blood and surgical instruments. Rectified04 contains 158 frames, and it appears to have slight camera motion. Rectified18 appears to contain more camera motion, so two subsets are chosen from the whole video with 113 frames in each. The frames are sampled at regular intervals

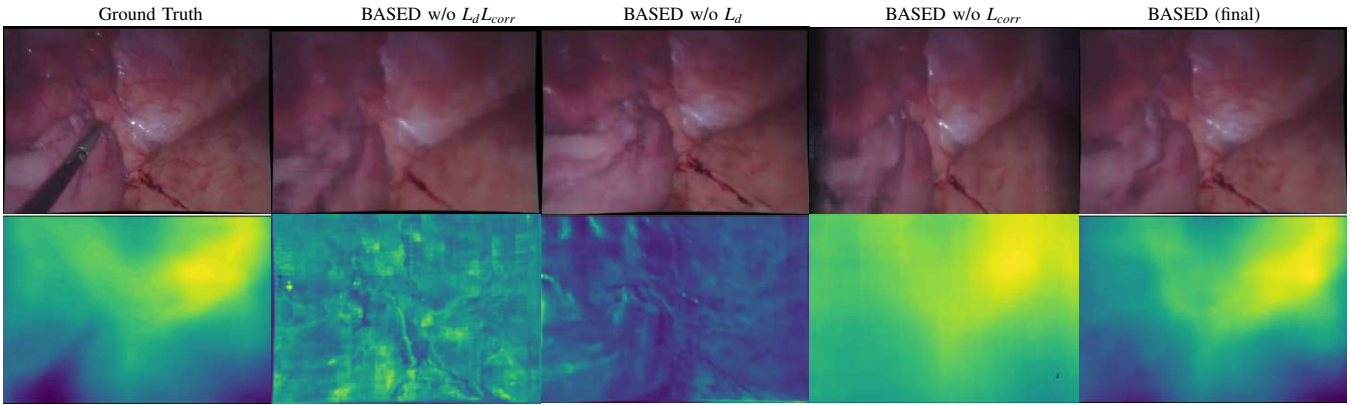


Fig. 4. Ablation analysis shows how different losses bring about an improvement in the rendered results from the final model. Please note that the depth in the Ground Truth column is the reference depth.

TABLE II. QUANTITATIVE ANALYSIS OF BASED AND CURRENT STATE-OF-THE-ART ON THE HAMLYN DATASET

	PSNR \uparrow			SSIM \uparrow			LPIPS \downarrow		
	EndoNeRF	RoDynRF	ours	EndoNeRF	RoDynRF	ours	EndoNeRF	RoDynRF	ours
Rectified04-1 (scds)	-	14.902	20.947	-	0.468	0.621	-	0.577	0.269
Rectified18-1 (mcDs)	22.838	25.700	32.277	0.817	0.874	0.944	0.273	0.192	0.106
Rectified18-2 (mcDs)	29.572	24.690	33.017	0.869	0.875	0.936	0.235	0.201	0.103

TABLE III. QUANTITATIVE ANALYSIS OF BASED AND CURRENT STATE-OF-THE-ART METHODS ON THE ENDONeRF DA VINCI DATASET [21] FOR STATIC SCENES WITH STEREO REFERENCE DEPTH.

	PSNR \uparrow			SSIM \uparrow			LPIPS \downarrow		
	EndoNeRF	RoDynRF	ours	EndoNeRF	RoDynRF	ours	EndoNeRF	RoDynRF	ours
pulling soft tissues	35.832	27.502	35.097	0.941	0.900	0.936	0.058	0.158	0.059
cutting tissues twice	35.720	21.105	35.706	0.935	0.700	0.934	0.063	0.280	0.073

(every 10 frames), as the original videos were too large. 10 percent of the total images were used for testing.

EndoNeRF Da Vinci dataset [21]: We used only two datasets used in the EndoNeRF paper that are publicly available. They last for 4-8 sec with 15 fps. Each of the videos is taken from a single static viewpoint setting. One of the videos demonstrates soft tissues being drastically pulled in 2 seconds, while the other video demonstrates soft tissue cutting with challenging topological changes. As mentioned in the original paper, the depth maps are obtained using STTR-LIGHT [41] from stereo images. The train-test split is the same as it is used in the original paper.

C. Metrics

We use (1) Peak Signal-to-Noise Ratio (PSNR), (2) Learned Perceptual Image Patch Similarity (LPIPS) [45], and (3) Structural Similarity Index (SSIM) [45] as the quantitative metrics.

D. Results

1) *Loss Ablations:* Table I and Figure 4 provide both quantitative and qualitative analysis of the effect of the various losses on the performance of our model. It shows that estimated depth guidance with our training scheme improves the reconstructed textures and depths significantly. Additionally, it shows that our correspondence loss leads

to better results. This indicates that the correspondence loss may have improved the estimated camera poses by instilling multi-view consistency in this dynamic deformable scene, which in turn leads to better convergence of the deformable NeRF model. However, the sequences are still severely underconstrained (camera movement/viewing angles of the scene are still limited in those sequences, which is common in surgical scenes), hence the correspondence loss only showed a slight improvement in depth reconstruction, which is not as dramatic as models using estimated depth loss. The tool masks for sequence - Rectified04-1 from the Hamlyn dataset does not always completely mask out the tools, which is why the resultant rendered images partially have tools in them (Figure 1), and not a transparent overlay like we see for the other rendered results.

2) *Comparison on Hamlyn dataset:* The main dataset we are evaluating is the Hamlyn dataset. We choose EndoNeRF and RoDynRF as our state-of-the-art comparisons for deformable scene reconstruction with obvious camera motions. We show in Figure 6 and Table II that our model outperforms both EndoNeRF and RoDynRF by a significant margin. The reason being that a major drawback of EndoNeRF is that it has only been tested for video sequences with single-view static cameras, which is severely under-constrained. In order to compare with EndoNeRF

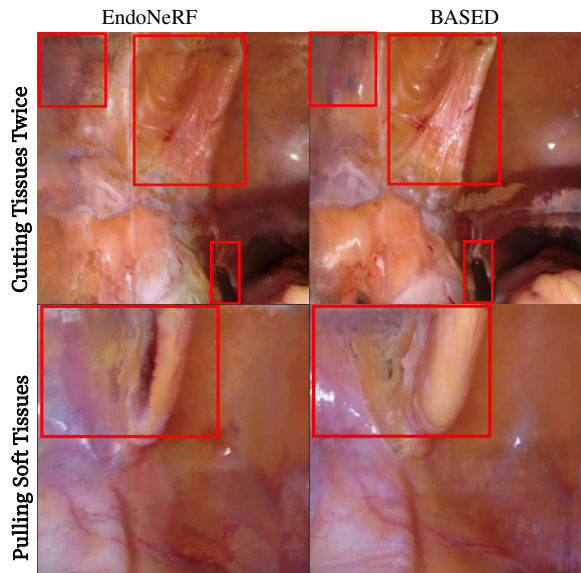


Fig. 5. Qualitative analysis of our proposed model BASED and EndoNeRF for novel view renderings. Highlighted sections show how BASED is able to avoid different artifacts in the images, resulting in a sharper image.

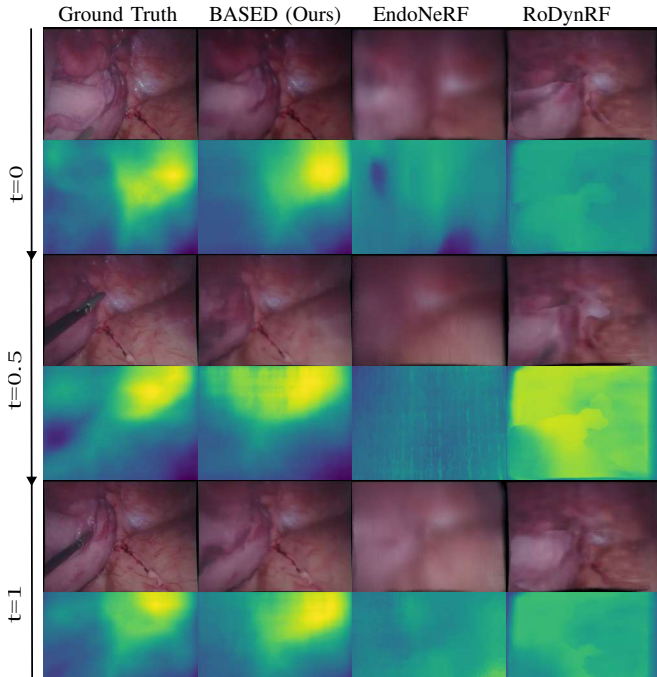


Fig. 6. Qualitative analysis of our proposed model BASED compared with RoDynRF and EndoNeRF (with COLMAP estimated poses) for sequences obtained from the public Hamlyn dataset. Please note that the depth in the Ground Truth column is the reference depth.

for sequences for dynamic scenes, we estimated camera poses using COLMAP. EndoNeRF fails when COLMAP fails to predict camera poses as seen for rectified04-1, thus automatically proving the superiority of our method. Even for sequences where COLMAP is able to estimate camera poses, we can see that our model BASED is able to model the dynamic and deformable aspects of the scene much better based on the quantitative and qualitative results.

Furthermore, we show that our methods can generalize toward surgical deformable scenes with stationary cameras. We evaluate our model on the sequences used in the EndoNeRF

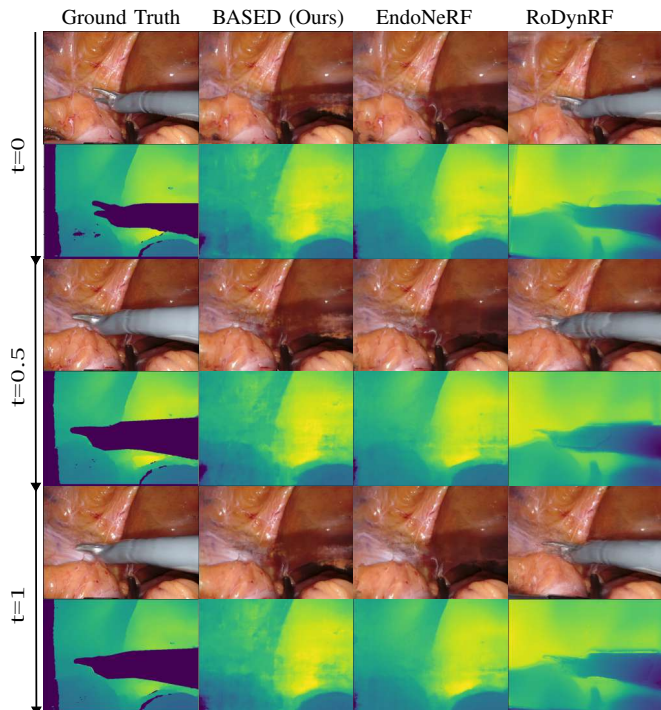


Fig. 7. Qualitative analysis of our proposed model BASED with RoDynRF and EndoNeRF for two publicly available sequences - "Cutting Tissues Twice"[21] guided by stereo depth.

paper: Cutting tissues twice and Pulling soft tissues. Table III and Figure 7 show a quantitative and qualitative evaluation of the performance of our model versus baseline EndoNeRF and RoDynRF. We can see that our model is on par, if not better than EndoNeRF, and performs significantly better than RoDynRF. In Figure 5, our model is able to generalize better to novel view renderings compared to EndoNeRF which has been strictly trained with static identity camera poses. Hence, our model retains EndoNeRF's capacity for static deformable monocular videos.

V. CONCLUSION

We propose BASED, a network that simultaneously estimates dynamic scene motions and reconstructs deformable surgical scenes from monocular videos. To the best of our knowledge, this is the first work that tries to reconstruct scenes from video sequences where the static and the dynamic parts cannot be clearly differentiated from one another, and also the first work that attempts to reconstruct deformable surgical scenes with unknown camera poses from monocular videos. Through our experiments, we have shown significant improvement over the existing state-of-the-art methods in this domain, and also potential for future research. Limitations of the presented model include slow optimization time (similar to EndoNeRF at several hours), though many recent strategies are drastically cutting this time by orders of magnitude (including ours [24]). Some potential future directions could be removing the dependency of BASED on reference depths, reducing optimization time, and automatic tool mask generation.

REFERENCES

- [1] M. Yip, S. Salcudean, K. Goldberg, K. Althoefer, A. Menciasci, J. D. Opfermann, A. Krieger, K. Swaminathan, C. J. Walsh, H. Huang, *et al.*, “Artificial intelligence meets medical robotics,” *Science*, vol. 381, no. 6654, pp. 141–146, 2023.
- [2] F. Liu, Z. Li, Y. Han, J. Lu, F. Richter, and M. C. Yip, “Real-to-sim registration of deformable soft tissue with position-based dynamics for surgical robot autonomy,” in *2021 IEEE International Conference on Robotics and Automation (ICRA)*, pp. 12328–12334, IEEE, 2021.
- [3] Y. Long, Z. Li, C. H. Yee, C. Ng, R. H. Taylor, M. Unberath, and Q. Dou, “E-DSSR: efficient dynamic surgical scene reconstruction with transformer-based stereoscopic depth perception,” *Med. Imag. Comput. Comput. Assis. Interv.*, 2021.
- [4] D. Recasens, J. Lamarca, J. M. Fácil, J. Montiel, and J. Civera, “Endo-depth-and-motion: Reconstruction and tracking in endoscopic videos using depth networks and photometric constraints,” *IEEE Int. Conf. Robot. Autom. Letters*, vol. 6, no. 4, pp. 7225–7232, 2021.
- [5] Z. Li, X. Liu, N. Drenkow, A. Ding, F. X. Creighton, R. H. Taylor, and M. Unberath, “Revisiting stereo depth estimation from a sequence-to-sequence perspective with transformers,” in *Int. Conf. Comput. Vis.*, pp. 6197–6206, October 2021.
- [6] K. L. Lurie, R. Angst, D. V. Zlatev, J. C. Liao, and A. K. Ellerbe Bowden, “3d reconstruction of cystoscopy videos for comprehensive bladder records,” *Biomed. Opt. Expr.*, pp. 2106–2123, 2017.
- [7] T. D. Soper, M. P. Porter, and E. J. Seibel, “Surface mosaics of the bladder reconstructed from endoscopic video for automated surveillance,” *IEEE Trans. Biomed. Eng.*, pp. 1670–1680, 2012.
- [8] M. Hu, G. Penney, M. Figl, P. Edwards, F. Bello, R. Casula, D. Rueckert, and D. Hawkes, “Reconstruction of a 3d surface from video that is robust to missing data and outliers: application to minimally invasive surgery using stereo and mono endoscopes,” *Medical Image Analysis*, 2012.
- [9] A. Resindra, Y. Monno, K. Imahori, M. Okutomi, S. Suzuki, T. Gotoda, and K. Miki, “3d reconstruction of whole stomach from endoscope video using structure-from-motion,” *IEEE Engi. Med. and Bio. Soci.*, vol. 2019, pp. 3900–3904, 07 2019.
- [10] T.-B. Phan, D.-H. Trinh, D. Wolf, and C. Daul, “Optical flow-based structure-from-motion for the reconstruction of epithelial surfaces,” *IEEE Conf. Comput. Vis. Pattern Recog.*, vol. 105, p. 107391, 2020.
- [11] A. R. Widya, Y. Monno, M. Okutomi, S. Suzuki, T. Gotoda, and K. Miki, “Whole stomach 3d reconstruction and frame localization from monocular endoscope video,” *IEEE J. Trans Engi. in Health and Medicine*, vol. 7, pp. 1–10, 2019.
- [12] J. Lamarca, S. Parashar, A. Bartoli, and J. M. M. Montiel, “DefSLAM: Tracking and mapping of deforming scenes from monocular sequences,” *IEEE Trans. Robot.*, vol. 37, pp. 291–303, February 2021.
- [13] J. J. G. Rodríguez, J. Lamarca, J. Morlana, J. D. Tardós, and J. M. Montiel, “Sd-defslam: Semi-direct monocular slam for deformable and intracorporeal scenes,” in *IEEE Int. Conf. Robot. Autom.*, pp. 5170–5177, 2021.
- [14] J. Song, J. Wang, L. Zhao, S. Huang, and G. Dissanayake, “Mislam: Real-time large scale dense deformable slam system in minimal invasive surgery based on heterogeneous computing,” *IEEE Int. Conf. Robot. Autom. Letters*, vol. PP, pp. 4068–4075, 03 2018.
- [15] O. Garcia-Grasa, E. Bernal, S. Casado, I. Gil, and J. Montiel, “Visual slam for handheld monocular endoscope,” *IEEE Trans. Med. Imag.*, vol. 33, pp. 135–146, 09 2013.
- [16] X. Liu, Z. Li, M. Ishii, G. D. Hager, R. H. Taylor, and M. Unberath, “Sage: Slam with appearance and geometry prior for endoscopy,” in *IEEE Int. Conf. Robot. Autom.*, pp. 5587–5593, 2022.
- [17] F. Richter, J. Lu, R. K. Orosco, and M. C. Yip, “Robotic tool tracking under partially visible kinematic chain: A unified approach,” *IEEE Transactions on Robotics*, vol. 38, no. 3, pp. 1653–1670, 2021.
- [18] “Auris health inc, johnson and johnson, monarch platform,” <https://www.jnjmedtech.com/en-us/product-family/monarch/>,” 2018.
- [19] “Endomaster pte ltd, endomaster ease system,” <http://www.endomastermedical.com/>,” 2018.
- [20] B. Mildenhall, P. P. Srinivasan, M. Tancik, J. T. Barron, R. Ramamoorthi, and R. Ng, “Nerf: Representing scenes as neural radiance fields for view synthesis,” in *Eur. Conf. Comput. Vis.*, 2020.
- [21] Y. Wang, Y. Long, S. H. Fan, and Q. Dou, “Neural rendering for stereo 3d reconstruction of deformable tissues in robotic surgery,” in *Med. Imag. Comput. Comput. Assis. Interv.*, pp. 431–441, Springer, 2022.

- [22] R. Zha, X. Cheng, H. Li, M. Harandi, and Z. Ge, "Endosurf: Neural surface reconstruction of deformable tissues with stereo endoscope videos," 2023.
- [23] Y. Chen and G. H. Lee, "Dbarf: Deep bundle-adjusting generalizable neural radiance fields," in *IEEE Conf. Comput. Vis. Pattern Recog.*, pp. 24–34, June 2023.
- [24] S. Liu, S. Lin, J. Lu, S. Saha, A. Supikov, and M. Yip, "Baa-ngp: Bundle-adjusting accelerated neural graphics primitives.," *arXiv*, 2023.
- [25] J. L. Schönberger and J.-M. Frahm, "Structure-from-motion revisited," in *Conference on Computer Vision and Pattern Recognition (CVPR)*, 2016.
- [26] J. L. Schönberger, E. Zheng, M. Pollefeys, and J.-M. Frahm, "Pixel-wise view selection for unstructured multi-view stereo," in *European Conference on Computer Vision (ECCV)*, 2016.
- [27] A. Pumarola, E. Corona, G. Pons-Moll, and F. Moreno-Noguer, "D-nerf: Neural radiance fields for dynamic scenes," *IEEE Conf. Comput. Vis. Pattern Recog.*, 2020.
- [28] Y.-L. Liu, C. Gao, A. Meuleman, H.-Y. Tseng, A. Saraf, C. Kim, Y.-Y. Chuang, J. Kopf, and J.-B. Huang, "Robust dynamic radiance fields," in *IEEE Conf. Comput. Vis. Pattern Recog.*, 2023.
- [29] C.-H. Lin, W.-C. Ma, A. Torralba, and S. Lucey, "Barf: Bundle-adjusting neural radiance fields," in *Int. Conf. Comput. Vis.*, 2021.
- [30] Y. Jeong, S. Ahn, C. Choy, A. Anandkumar, M. Cho, and J. Park, "Self-calibrating neural radiance fields," in *Int. Conf. Comput. Vis.*, 2021.
- [31] P. Truong, M.-J. Rakotosaona, F. Manhardt, and F. Tombari, "Sparf: Neural radiance fields from sparse and noisy poses," in *IEEE Conf. Comput. Vis. Pattern Recog.*, 2023.
- [32] S.-F. Chng, S. Ramasinghe, J. Sherrah, and S. Lucey, "Gaussian activated neural radiance fields for high fidelity reconstruction and pose estimation," in *Eur. Conf. Comput. Vis.*, 2022.
- [33] Z. Cheng, C. Esteves, V. Jampani, A. Kar, S. Maji, and A. Makadia, "Lu-nerf: Scene and pose estimation by synchronizing local unposed nerfs," 2023.
- [34] Y. Xia, H. Tang, R. Timofte, and L. V. Gool, "Sinerf: Sinusoidal neural radiance fields for joint pose estimation and scene reconstruction," in *33rd British Machine Vision Conference 2022, BMVC 2022, London, UK, November 21-24, 2022*, Brit. Mach. Vis. Ass., 2022.
- [35] W. Bian, Z. Wang, K. Li, J. Bian, and V. A. Prisacariu, "Nope-nerf: Optimising neural radiance field with no pose prior," *IEEE Conf. Comput. Vis. Pattern Recog.*, 2023.
- [36] A. Meuleman, Y.-L. Liu, C. Gao, J.-B. Huang, C. Kim, M. H. Kim, and J. Kopf, "Progressively optimized local radiance fields for robust view synthesis," in *IEEE Conf. Comput. Vis. Pattern Recog.*, 2023.
- [37] C. Gao, A. Saraf, J. Kopf, and J.-B. Huang, "Dynamic view synthesis from dynamic monocular video," in *Int. Conf. Comput. Vis.*, 2021.
- [38] W. Abdulla, "Mask r-cnn for object detection and instance segmentation on keras and tensorflow," 2017.
- [39] Z. Teed and J. Deng, "Raft: Recurrent all-pairs field transforms for optical flow," in *Eur. Conf. Comput. Vis.*, 2020.
- [40] P. Truong, M. Danelljan, L. Van Gool, and R. Timofte, "Learning accurate dense correspondences and when to trust them," in *Proceedings of the IEEE/CVF Conference on Computer Vision and Pattern Recognition*, pp. 5714–5724, 2021.
- [41] Z. Li, X. Liu, N. Drenkow, A. Ding, F. X. Creighton, R. H. Taylor, and M. Unberath, "Revisiting stereo depth estimation from a sequence-to-sequence perspective with transformers," in *Proceedings of the IEEE/CVF international conference on computer vision*, pp. 6197–6206, 2021.
- [42] A. Kirillov, E. Mintun, N. Ravi, H. Mao, C. Rolland, L. Gustafson, T. Xiao, S. Whitehead, A. C. Berg, W.-Y. Lo, P. Dollár, and R. Girshick, "Segment anything," *arXiv*, 2023.
- [43] P. Truong, M. Danelljan, L. V. Gool, and R. Timofte, "Learning accurate dense correspondences and when to trust them," *IEEE Conf. Comput. Vis. Pattern Recog.*, pp. 5714–5724, 2021.
- [44] L. Xi, Y. Zhao, L. Chen, Q. H. Gao, W. Tang, T. R. Wan, and T. Xue, "Recovering dense 3d point clouds from single endoscopic image," *Computer Methods and Programs in Biomedicine*, vol. 205, p. 106077, 2021.
- [45] R. Zhang, P. Isola, A. A. Efros, E. Shechtman, and O. Wang, "The unreasonable effectiveness of deep features as a perceptual metric," in *Proceedings of the IEEE conference on computer vision and pattern recognition*, pp. 586–595, 2018.